

Sparse but not Simpler: A Multi-Level Interpretability Analysis of Vision Transformers

Siyu Zhang¹

University of Texas at Austin, Austin TX 78712, USA

Abstract. Sparse neural networks are often hypothesized to be more interpretable than dense models, motivated by findings that weight sparsity can produce compact circuits in language models. However, it remains unclear whether structural sparsity itself leads to improved semantic interpretability. In this work, we systematically evaluate the relationship between weight sparsity and interpretability in Vision Transformers using DeiT-III B/16 models pruned with Wanda. To assess interpretability comprehensively, we introduce **IMPACT**, a multi-level framework that evaluates interpretability across four complementary levels: neurons, layer representations, task circuits, and model-level attribution. Layer representations are analyzed using BatchTopK sparse autoencoders, circuits are extracted via learnable node masking, and explanations are evaluated with transformer attribution using insertion and deletion metrics. Our results reveal a clear structural effect but limited interpretability gains. Sparse models produce circuits with approximately $2.5\times$ fewer edges than dense models, yet the fraction of active nodes remains similar or higher, indicating that pruning redistributes computation rather than isolating simpler functional modules. Consistent with this observation, sparse models show no systematic improvements in neuron-level selectivity, SAE feature interpretability, or attribution faithfulness. These findings suggest that structural sparsity alone does not reliably yield more interpretable vision models, highlighting the importance of evaluation frameworks that assess interpretability beyond circuit compactness.

Keywords: mechanistic interpretability · feature representation

1 Introduction

Understanding how neural networks internally compute their predictions is a central goal of mechanistic interpretability [6, 27]. While substantial progress has been made in analyzing language models, interpreting large-scale vision models such as Vision Transformers (ViTs) remains challenging due to their highly distributed representations and complex internal computations.

One promising direction is to introduce *sparsity*. The intuition is that if a model relies on fewer connections, its computations may be easier to trace and its internal circuits easier to analyze. This idea has long been explored in model compression [19, 24] and has recently gained traction in mechanistic interpretability. In particular, Gao *et al.* [22] showed that weight-sparse transformers trained

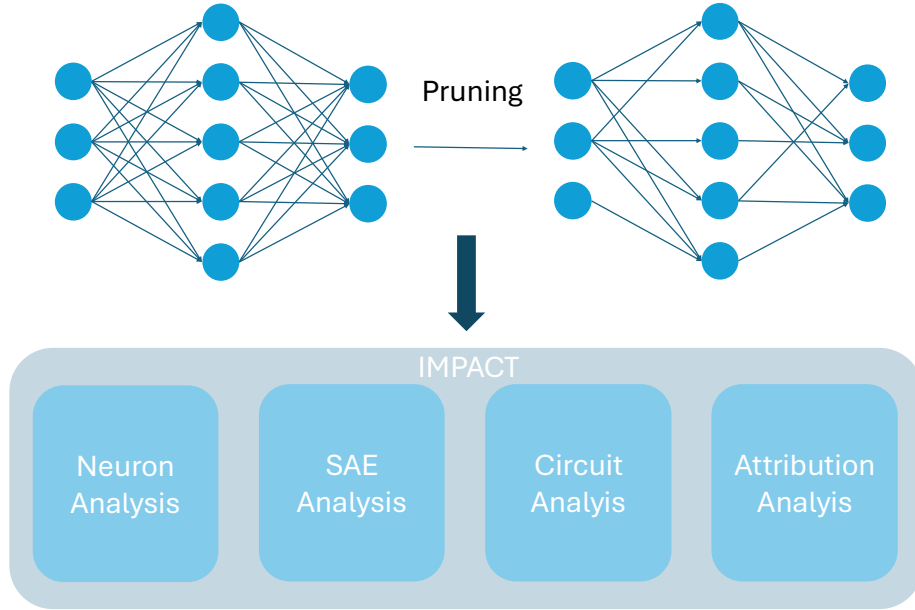


Fig. 1: The IMPACT (Interpretability Multi-level Pipeline for Assessing Computational Transparency) framework used to evaluate interpretability across four levels of analysis.

on algorithmic language tasks exhibit compact circuits implementing behaviors such as pattern matching and string completion. Their results suggest that increasing sparsity can produce smaller computational subgraphs that are easier to study.

However, existing evidence for the sparsity–interpretability connection is largely based on *structural* metrics, such as circuit size. Smaller circuits are often assumed to be more interpretable. Yet structural simplicity does not necessarily imply semantic clarity: neurons may remain polysemantic, learned features may not align with human concepts, and attribution maps may not become more faithful. Furthermore, most empirical studies focus on language models solving relatively simple tasks. Whether sparsity provides similar interpretability benefits for vision models operating on natural images remains unclear.

To address these questions, we perform a systematic comparison between dense and sparse Vision Transformers and evaluate interpretability across multiple levels of analysis. We introduce **IMPACT** (Interpretability Multi-level Pipeline for Assessing Computational Transparency), a framework that measures interpretability at four complementary levels:

Neuron level. We measure neuron-level interpretability using four metrics: selectivity, ablation impact, class variance, and label entropy (Sec. 3.2).

Layer level. We analyze intermediate representations using sparse autoencoders [9], comparing reconstruction quality and feature interpretability between dense and sparse models (Sec. 3.3).

Circuit level. Following Gao *et al.* [22], we extract minimal circuits responsible for single-category prediction across 100 ImageNet classes and compare their structural properties, including edge count, node usage, and a proposed Normalized Circuit Quality metric (Sec. 3.4).

Model level. We evaluate the faithfulness of input attribution maps using transformer attribution [12], together with insertion and deletion metrics [31] (Sec. 3.5).

As shown in Fig. 1, we first construct sparse models using weight pruning methods. Both the original dense model and the pruned models are then evaluated using the IMPACT framework.

All experiments are conducted on DeiT-III B/16 [36], a strong supervised ViT baseline, and its sparse variants obtained via Wanda pruning [33] followed by fine-tuning.

Our results reveal a nuanced relationship between sparsity and interpretability. At the circuit level, sparse models indeed produce structurally smaller circuits: dense models contain approximately $2.6\times$ more edges than their 70%-sparse counterparts. However, the number of active nodes does not decrease correspondingly, indicating that pruning redistributes computation across a similar number of components rather than isolating simpler modules. Consistent with this observation, we find no meaningful improvements in neuron-level selectivity, sparse autoencoder feature interpretability, or attribution faithfulness. These results suggest that structural sparsity alone does not guarantee improved interpretability in vision models.

Contributions. This work makes three contributions:

1. We provide a systematic comparison of interpretability in dense and sparse Vision Transformers, extending sparse circuit analysis from language models to the vision domain.
2. We introduce the IMPACT framework, a multi-level evaluation pipeline that measures interpretability at the neuron, layer, circuit, and model levels, together with a Normalized Circuit Quality metric for assessing circuit compactness and fidelity.
3. Our experiments show that while sparsity reduces circuit edge counts by up to $2.5\times$, it does not improve neuron-level selectivity, SAE feature interpretability, or attribution faithfulness, challenging the assumption that structural sparsity implies mechanistic transparency.

2 Related Work

Mechanistic Interpretability and Circuits. Mechanistic interpretability seeks to reverse-engineer neural networks into human-understandable features and circuits [27]. Early work identified curve and frequency detectors in convolutional

networks [10, 32, 38]. Subsequent research extended these ideas to Transformers by analyzing attention patterns and residual streams [17], revealing mechanisms such as induction heads [28] and indirect object identification circuits [39]. Recent automated approaches aim to scale circuit discovery [7, 13]. However, circuits extracted from dense models often remain large and difficult to interpret due to extensive polysemanticity [11].

Interpretability in Vision Transformers. Applying mechanistic interpretability to vision models introduces additional challenges. Vision Transformers (ViTs) process continuous and highly correlated image patches [15], in contrast to the discrete token sequences used in language models. Early interpretability work therefore focused primarily on attention visualization and rollout methods [1]. More recent studies have begun analyzing residual streams and module-level computations in ViTs [5, 34]. Representation structure is also shaped by the training objective: self-supervised vision models often exhibit emergent segmentation behavior, while supervised models such as DeiT primarily optimize class discrimination, leading to highly polysemantic internal features. This makes supervised ViTs a useful setting for studying whether architectural interventions, such as pruning, can encourage more interpretable representations.

Superposition and Sparse Autoencoders. Neural networks frequently represent more features than neurons through superposition [16]. Sparse autoencoders (SAEs) attempt to disentangle these representations by decomposing activations into sparse latent features [8, 14]. Recent work has scaled SAEs to large models [23, 35] and proposed architectural improvements including Gated [29], JumpReLU [30], and BatchTopK [9] variants. These methods have enabled feature-level circuit analysis and attribution graph construction [4, 25]. In this work we employ BatchTopK SAEs to investigate a comparative question: whether weight-sparse models produce more disentangled activation features than dense models.

Weight Pruning and Interpretability. Weight pruning was originally developed to improve model efficiency [24]. The Lottery Ticket Hypothesis [19] later suggested that sparse subnetworks may capture meaningful computational structure. Modern one-shot pruning methods such as SparseGPT [20] and Wanda [33] enable high sparsity with limited performance degradation. Recent work has begun exploring connections between sparsity and interpretability. For example, Gao *et al.* [22] found that weight-sparse Transformers produce simpler circuits for algorithmic tasks, though their study focused on small language models and circuit-level analysis only. In parallel, Zimmermann *et al.* [40] observed that increasing model scale alone does not improve mechanistic interpretability in vision models. Our work bridges these directions by systematically evaluating whether weight sparsity improves interpretability in vision Transformers across multiple levels of analysis.

Transformer Attribution. Attribution methods for Vision Transformers have evolved from class-agnostic attention rollout [1] to gradient-based approaches

that incorporate model structure. Chefer *et al.* [12] proposed a gradient-weighted attention formulation combined with Layer-wise Relevance Propagation (LRP) to properly handle residual connections in ViTs, with subsequent refinements improving stability and faithfulness [2, 3]. We adopt the method of Chefer *et al.* for its established empirical reliability and evaluate attribution quality using insertion and deletion metrics [31].

3 Methods

We introduce the IMPACT framework to compare the interpretability of dense and sparse Vision Transformers across complementary levels: neuron (Sec. 3.2), layer (Sec. 3.3), circuit (Sec. 3.4), and model (Sec. 3.5). Interpretability can manifest at multiple scales within a neural network, ranging from individual units to task-level behavior. Improvements at one level do not necessarily imply improvements at another; for example, a model may exhibit smaller circuits while still maintaining highly polysemantic neurons or entangled representations. Evaluating interpretability across multiple levels therefore provides a more comprehensive view of how sparsity affects internal representations and model explanations. We begin by describing the construction of our sparse models (Sec. 3.1).

3.1 Sparse Model Construction

We use DeiT-III B/16 [36] as our backbone architecture. To construct sparse variants, we compare standard magnitude pruning [24] with **Wanda** [33], which scores each weight using the product of its magnitude and the corresponding input activation norm:

$$S_{ij} = |W_{ij}| \cdot \|X_j\|_2. \quad (1)$$

Weights with the lowest scores within each output row are pruned to zero. After pruning, all sparse models are fine-tuned on ImageNet-1K to recover performance.

3.2 Neuron-Level Interpretability

The neuron level evaluates whether sparsity leads to more faithful or less polysemantic representations. We analyze individual neurons using four complementary metrics.

Ablation Impact. Ablation impact measures *functional concentration*: do the most important neurons account for a larger share of the model’s computation in sparse networks? We simultaneously ablate the top- K neurons by replacing their activations with their dataset mean and measure the normalized logit change [37]:

$$\text{Abl}(\ell, c) = \frac{f_c(x) - f_c^{\text{abl}}(x)}{\|f(x)\|}. \quad (2)$$

Higher values indicate that the selected neurons contribute a larger fraction of the class-relevant signal.

Selectivity. Selectivity measures the degree to which a neuron correlates with a specific class label. We compute the AUROC of each neuron’s CLS-token activation as a binary classifier for the target class [18]:

$$\text{Selectivity}(n, c) = \text{AUROC}(a_n^{\text{CLS}}(x), y_c(x)). \quad (3)$$

An AUROC of 1.0 indicates perfect class selectivity, while 0.5 indicates no discriminative power.

Class Variance. Class variance provides an estimate of polysemanticity by measuring response consistency within a class. For each neuron we compute the coefficient of variation of per-image maximum patch activations:

$$\text{CV}(n, c) = \frac{\sigma(\{m_n(x)\}_{x \in D_c})}{\mu(\{m_n(x)\}_{x \in D_c})}, \quad (4)$$

where

$$m_n(x) = \max_{t \in \text{patches}} a_n^t(x). \quad (5)$$

Lower values indicate neurons that respond consistently across images of the same class.

Label Entropy. Label entropy measures monosemanticity by quantifying how broadly a neuron responds across classes. We compute the Shannon entropy over each neuron’s class activation distribution [21]:

$$H(n) = - \sum_c P_n(c) \log P_n(c), \quad (6)$$

where

$$P_n(c) = \frac{\sum_{x \in D_c} m_n(x)}{\sum_{c'} \sum_{x \in D_{c'}} m_n(x)}. \quad (7)$$

Lower entropy indicates neurons that respond predominantly to a single class. We report averages over the top- K neurons and 100 ImageNet categories for each layer and sparsity level.

3.3 Layer-Level Interpretability

While individual neurons often multiplex multiple concepts, layer-level interpretability seeks to disentangle these representations at the representation level. We evaluate this using Sparse Autoencoders (SAEs), which act as analytical probes for decomposing dense activations into sparse features.

To isolate the effect of model sparsity from SAE optimization artifacts (such as feature shrinkage or latent collapse), we adopt BatchTopK SAEs [9]. Given an activation $\mathbf{x} \in \mathbb{R}^n$, the encoder produces sparse features

$$\mathbf{f}(\mathbf{x}) = \text{BatchTopK}(W_{\text{enc}}\mathbf{x} + \mathbf{b}_{\text{enc}}), \quad (8)$$

and reconstructs the activation as

$$\hat{\mathbf{x}} = W_{\text{dec}}\mathbf{f}(\mathbf{x}) + \mathbf{b}_{\text{dec}}. \quad (9)$$

The model is trained to minimize reconstruction error $\|\mathbf{x} - \hat{\mathbf{x}}\|_2^2$.

SAE Quality. We measure reconstruction fidelity using normalized mean squared error (NMSE), the fraction of dead latents, and the fraction of explained variance.

Feature Interpretability. To evaluate whether sparsity reduces superposition, we apply the same four metrics from Sec. 3.2—mean ablation impact, selectivity, class variance, and label entropy—to the learned SAE features. Each latent dimension is treated as a fundamental unit of analysis analogous to a neuron.

3.4 Circuit-Level Interpretability

The circuit level evaluates interpretability at the task level. For image classification models, extracting circuits for a “single-category versus rest” prediction provides a natural and tractable task. For each category, we identify minimal functional circuits in both dense and sparse models by learning which computational nodes are necessary for the target prediction.

Node Definition and Masking. Following Gao *et al.* [22], we insert learnable masks at multiple locations within each transformer block: after each LayerNorm in the attention and MLP sub-blocks, after the attention $q/k/v$ projections, after each MLP activation, and at the output of each sub-block before the residual addition. Each mask element corresponds to a *node*, and the mask determines whether the node participates in the active circuit. Masks are applied uniformly across tokens and images.

Optimization. Each node is associated with a continuous parameter constrained to $[-1, 1]$. This parameter is converted into a binary mask via the Heaviside step function, implemented with a sigmoid straight-through estimator to enable backpropagation. Parameters are initialized with scaled Gaussian noise and optimized using AdamW with linear learning rate decay. The objective combines task loss with a sparsity penalty:

$$\mathcal{L}_{\text{circuit}} = \mathcal{L}_{\text{task}}(\tilde{\mathbf{a}}, c) + k \cdot |\{i : m_i > 0\}|. \quad (10)$$

Inactive nodes are not zeroed out but replaced with their mean activation over the training distribution:

$$\tilde{\mathbf{a}}_\ell = \mathbf{m}_\ell \odot \mathbf{a}_\ell + (1 - \mathbf{m}_\ell) \odot \bar{\mathbf{a}}_\ell. \quad (11)$$

Normalized Circuit Quality (NCQ). Existing work typically reports absolute circuit size, which can bias comparisons against dense models. To jointly evaluate fidelity and compactness, we introduce the Normalized Circuit Quality metric:

$$\text{NCQ}(c) = \frac{\text{Acc}_{\text{circuit}}(c)}{\text{Acc}_{\text{full}}(c)} \left(1 - \frac{|\mathcal{N}_{\text{circuit}}(c)|}{|\mathcal{N}_{\text{total}}|} \right). \quad (12)$$

The first factor measures fidelity (accuracy retained relative to the full model), while the second measures compression (the fraction of nodes removed). NCQ $\in [0, 1]$ is maximized when a circuit is both faithful and compact.

3.5 Model-Level Interpretability

Finally, we evaluate interpretability at the model level, which reflects the end-to-end explainability of the network’s predictions. While the previous levels analyze internal components, this level asks whether sparsity improves the interpretability of the model’s final decisions.

Transformer Attribution. We adopt the attribution method of Chefer *et al.* [12], which combines gradient-weighted attention with LRP-style relevance propagation across transformer layers. Unlike attention rollout [1], this method produces class-specific explanations and properly handles skip connections while preserving relevance conservation.

Faithfulness Evaluation. Attribution maps can appear visually plausible while remaining unfaithful. We therefore evaluate attribution quality using the standard **insertion** and **deletion** metrics [31] with a zero-valued reference image.

Insertion (AUC \uparrow) progressively reveals pixels in order of decreasing relevance starting from a blank image, measuring the area under the predicted class probability curve.

Deletion (AUC \downarrow) progressively removes pixels in the same order and measures the resulting confidence curve. A faithful attribution map should cause a rapid drop in model confidence.

4 Experiments

All experiments are conducted on ImageNet-1K using DeiT-III B/16 as the base architecture. We first examine the accuracy–sparsity trade-off to determine an appropriate operating point (Sec. 4.1). We then evaluate interpretability using the IMPACT framework across four complementary levels: neuron (Sec. 4.2), layer (Sec. 4.3), circuit (Sec. 4.4), and model (Sec. 4.5). Neuron-, layer-, and model-level analyses are performed across all ImageNet categories, while the computationally intensive circuit extraction is conducted on a representative subset of 100 categories.

4.1 Sparsity vs. Accuracy

Tab. 1 reports ImageNet-1K accuracy for DeiT-III B/16 across sparsity levels ranging from 10% to 90%, comparing magnitude pruning and Wanda, each followed by two epochs of fine-tuning.

Both pruning methods maintain near-dense accuracy at moderate sparsity levels (up to 50%). Their performance remains nearly identical through 70% sparsity, where Wanda exceeds magnitude pruning by only 0.18%. The gap becomes more pronounced at extreme sparsity: at 90%, Wanda retains 61.51% top-1 accuracy compared to 55.17% for magnitude pruning.

Table 1: Accuracy comparison of pruning methods on DeiT-III B/16. Wanda shows slightly stronger performance recovery, particularly at high sparsity. Accuracy degrades substantially beyond the 0.7 sparsity threshold.

Method	Metric	Sparsity Ratio						
		0.0 (Dense)	0.1	0.3	0.5	0.7	0.8	0.9
Magnitude	Top-1	0.8371	0.8152	0.8173	0.8159	0.8026	0.7661	0.5517
	Top-5	0.9655	0.9565	0.9572	0.9563	0.9498	0.9313	0.7873
Wanda	Top-1	0.8371	0.8154	0.8174	0.8158	0.8044	0.7687	0.6151
	Top-5	0.9655	0.9563	0.9564	0.9565	0.9510	0.9343	0.8426

Because accuracy degrades sharply beyond the 70% threshold, we select **70% Wanda sparsity** as our primary operating point. At this level, the model preserves over 96% of the dense network’s top-1 accuracy while removing a substantial fraction of weights. This allows us to study the interpretability effects of sparsity without confounding results with severe performance degradation. Since both pruning methods yield nearly identical accuracy at this sparsity level, our subsequent interpretability analysis focuses on Wanda-pruned models and is unlikely to be sensitive to the choice of pruning algorithm.

4.2 Neuron-Level Results

Setup. For each of the 1,000 ImageNet categories, we identify the top-50 most important neurons at early (block 2), middle (block 7), and late (block 11) layers using attribution patching [26]. We compute all four neuron-level metrics at sparsity levels $\{0.1, 0.3, 0.5, 0.7\}$. To accurately reflect the baseline functional state of the network, all neuron-level ablations use *mean ablation*.

Results. Fig. 2 shows violin plots for each metric across layers and sparsity levels, with distributions aggregated over all ImageNet categories. Overall, the relationship between sparsity and the four interpretability metrics is weak and inconsistent.

In the early and middle layers of the 70% sparse model, we observe a small number of categories with unusually high mean ablation scores. This suggests that, for a limited subset of tasks, extreme sparsity may force the model to route critical computation through a small number of neurons. However, this behavior appears only in a narrow tail of the distribution and does not generalize.

In the late layers, both dense and sparse models exhibit occasional outliers with high ablation scores, indicating that the most important neurons in the final blocks can strongly influence predictions regardless of sparsity level. While the sparse model shows slightly higher sensitivity in block 11, the difference is small and does not systematically correlate with increasing sparsity.

Across the majority of categories, we observe no consistent changes in selectivity, label entropy, or class variance. In particular, label entropy remains high

and class variance remains stable across sparsity levels, indicating that neurons in sparse models remain similarly polysemantic to those in dense models. These results suggest that weight sparsity alone does not significantly reduce neuron-level feature multiplexing nor change how semantic information is distributed across neurons.

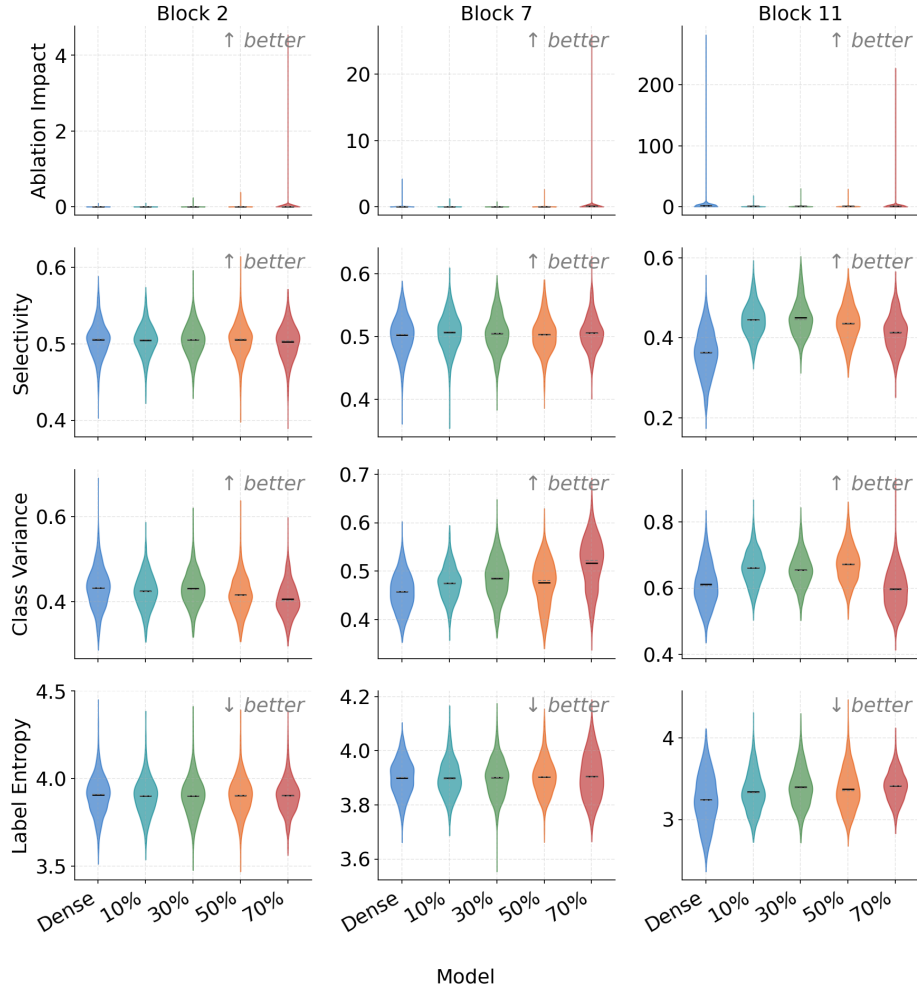


Fig. 2: Neuron-level interpretability metrics across layers (columns) and sparsity levels (colors). Each distribution spans all 1,000 ImageNet categories.

4.3 Layer-Level Results

We train BatchTopK SAEs with $k = 128$ and an expansion factor of 32 on the residual stream of the final transformer block (block 11). Because SAE latents are

Table 2: SAE reconstruction quality for block 11 activations.

Sparsity	NMSE ↓	Dead ↓	Expl. Var. (%) ↑
Dense (0%)	0.0075	85.93	99.25
10%	0.0404	74.97	95.96
30%	0.0396	75.18	96.04
50%	0.0461	72.96	95.39
70%	0.0594	68.31	94.06

explicitly designed to be sparse with a natural “off” state, we use *zero ablation* for all SAE feature evaluations, in contrast to the mean ablation used at the neuron level.

SAE Reconstruction Quality. Tab. 2 reports reconstruction metrics at each sparsity level. The dense model achieves the lowest NMSE (0.0075), while NMSE increases as sparsity grows, reaching 0.0594 at 70% sparsity. In parallel, though we can see a decrease in dead features with sparsity, the actual number comparing to total features is extremely small and the changes are negligible.

Together, these trends suggest that SAEs trained on sparse-model activations rely on a broader set of active latents to achieve reconstruction, consistent with a more distributed representation at high sparsity.

SAE Feature Interpretability. Fig. 3 summarizes the four interpretability metrics applied to SAE features in block 11 across sparsity levels. We observe two non-monotonic effects. First, at 10% sparsity, SAE features exhibit higher selectivity and class variance relative to the dense baseline. One plausible explanation is that light pruning acts as a regularizer, removing some redundant connections and slightly sharpening a subset of features. However, this effect does not persist at higher sparsity levels (30%–70%).

Overall, these layer-level results align with our neuron-level findings: SAE features trained on sparse activations are not consistently more selective, monosemantic, or class-consistent than those trained on dense activations. In particular,

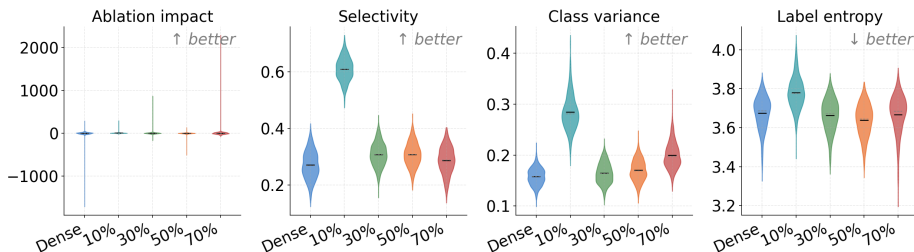
**Fig. 3: SAE feature interpretability** for block 11 across sparsity levels.

Table 3: Circuit-level comparison across sparsity levels, averaged over 100 ImageNet categories (mean \pm std). While sparse models use a larger fraction of their remaining nodes, overall circuit edge size decreases with sparsity, yielding higher NCQ.

Model	Node (%)	Size (%) \downarrow	Acc. (%) \uparrow	NCQ \uparrow
Dense	29.03 \pm 1.97	32.42 \pm 1.75	89.12 \pm 6.58	0.602 \pm 0.046
Wanda 10%	36.43 \pm 1.63	34.23 \pm 0.98	92.32 \pm 3.86	0.607 \pm 0.028
Wanda 30%	36.42 \pm 1.74	26.89 \pm 0.77	92.31 \pm 4.44	0.675 \pm 0.035
Wanda 50%	37.83 \pm 1.75	19.90 \pm 0.61	90.82 \pm 5.81	0.727 \pm 0.047
Wanda 70%	41.60 \pm 2.23	12.94 \pm 0.58	89.64 \pm 6.22	0.780 \pm 0.054

increasing weight sparsity does not yield systematic improvements in feature superposition as measured by our metrics.

4.4 Circuit-Level Results

Setup. Because circuit extraction is computationally expensive, we evaluate a representative subset of 100 ImageNet categories spanning 13 semantic groups. We extract minimal circuits from the dense model and Wanda-pruned models at sparsity levels $\{0.1, 0.3, 0.5, 0.7\}$. We report two size measures: *node fraction* (the percentage of computational nodes active in the circuit) and *circuit size* (the percentage of total edges remaining in the network), along with circuit accuracy and NCQ (Eq. (12)).

Circuit extraction is the only level at which sparsity yields a clear reduction in structural size. As shown in Tab. 3, circuit edge size decreases with sparsity: the 70%-sparse model requires 12.94% of total edges to predict a category, compared to 32.42% for the dense model (a $2.5\times$ reduction). Circuit accuracy remains close to 90% across settings, and NCQ increases from 0.602 (dense) to 0.780 (70% sparse).

However, this reduction in edge count should be interpreted cautiously. Because sparse models already contain far fewer parameters, any extracted sub-circuit is constrained to operate within a smaller pool of available edges. As a result, lower circuit edge counts partly reflect the underlying sparsity of the architecture rather than an intrinsic improvement in interpretability.

The *node fraction* provides additional insight. Although sparse circuits contain fewer edges overall, they recruit a larger fraction of the available computational nodes (41.60% at 70% sparsity vs. 29.03% for the dense model). This indicates that pruning reduces connectivity but does not necessarily concentrate computation into fewer functional units.

We refer to this effect as *representation spreading*. While pruning removes many edges, it also reduces the capacity of individual neurons, causing the model to distribute computation across more surviving components. As a result, structural sparsity reduces edge counts but does not necessarily simplify the underlying predictive logic.

Table 4: Attribution faithfulness. Evaluated over all ImageNet categories. A faithful attribution should yield high insertion AUC and low deletion AUC.

Sparsity	Dense	10%	30%	50%	70%
Insertion ↑	0.600	0.703	0.714	0.706	0.663
Deletion ↓	0.212	0.201	0.200	0.203	0.175

4.5 Model-Level Results

Quantitative Results. Tab. 4 reports insertion and deletion AUC, averaged over all ImageNet categories.

Introducing sparsity yields an initial improvement in attribution faithfulness. Relative to the dense model, 10% sparsity increases insertion to 0.703 and slightly reduces deletion to 0.201, with insertion peaking at 0.714 at 30% sparsity while deletion remains around 0.200. Beyond this point the trend does not persist: insertion declines to 0.706 at 50% and further to 0.663 at 70%, although deletion improves to 0.175 at the highest sparsity. Overall, these results suggest that light pruning may provide modest gains, but attribution faithfulness does not improve consistently as sparsity increases.

Qualitative Results. Fig. 4 shows attribution maps for selected categories across sparsity levels.

The qualitative examples broadly match the quantitative trends. Across categories, sparse models do not consistently produce better spatial localization or clearer semantic grounding. In some cases, sparsity yields slightly sharper maps (e.g., *telescope* and *gorilla*), but this effect is not consistent across examples.

5 Discussion and Conclusion

In this work, we investigated whether structural sparsity improves mechanistic interpretability in Vision Transformers. Using the IMPACT framework, we performed a multi-level analysis comparing dense and sparse models across neuron-, layer-, circuit-, and model-level interpretability metrics. Our results show that structural sparsity and semantic interpretability do not necessarily align.

Circuit Size vs. Functional Simplicity. At the circuit level, sparse models yield substantially smaller circuits: at 70% sparsity, extracted circuits contain approximately 2.5× fewer edges than those from dense models. However, sparse circuits recruit a larger fraction of their remaining computational nodes, indicating that pruning reduces connectivity without concentrating computation into fewer functional components.

Persistent Feature Entanglement. At both the neuron and layer (SAE) levels, sparse models exhibit similar selectivity, entropy, and response variance as dense models. Neurons and SAE features remain highly polysemantic, suggesting that sparsity alone does not meaningfully reduce representational superposition.

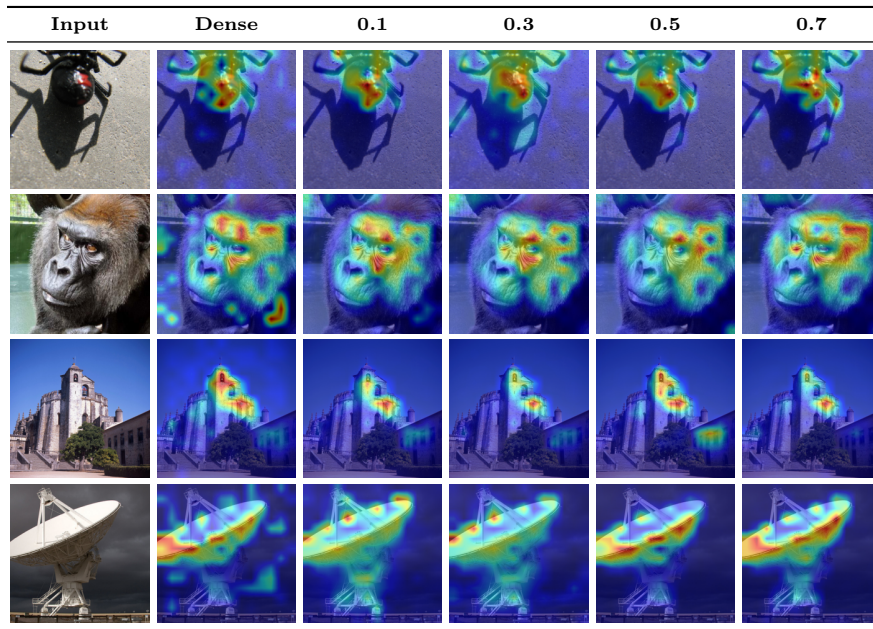


Fig. 4: Visual attribution comparing the dense DeiT3-B/16 model against models with sparsities of 0.1, 0.3, 0.5, and 0.7.

Model-Level Explanations. At the model level, attribution metrics show only modest improvements at low sparsity, likely reflecting a mild regularization effect. As sparsity increases, attribution quality remains largely unchanged, and qualitative visualizations show no consistent improvement in spatial localization.

Limitations and Future Directions. Our analysis has several limitations. First, the sparse models studied here are obtained via post-hoc pruning rather than trained as sparse networks from scratch, which may lead to different representational dynamics. Second, our evaluation relies on proxy measures of polysemanticity and superposition (e.g., selectivity, entropy, and SAE features) rather than ground-truth concept annotations. Future work could explore additional quantitative evaluation methods, such as concept probing or linear probing, to better characterize the semantic information encoded in sparse representations. Finally, our experiments focus on supervised Vision Transformers trained on ImageNet; interpretability behavior may differ in other training regimes such as self-supervised or multimodal models.

Implications. While pruning methods such as Wanda can reduce parameter counts while preserving accuracy, they do not inherently promote more modular or disentangled representations. Improving interpretability may therefore require training objectives or architectural priors that explicitly encourage semantic structure, rather than relying solely on post-hoc sparsification.

References

1. Abnar, S., Zuidema, W.: Quantifying attention flow in transformers. In: Proceedings of the 58th annual meeting of the association for computational linguistics. pp. 4190–4197 (2020)
2. Achtibat, R., Hatefi, S.M.V., Dreyer, M., Jain, A., Wiegand, T., Lapuschkin, S., Samek, W.: Attnlrp: attention-aware layer-wise relevance propagation for transformers. arXiv preprint arXiv:2402.05602 (2024)
3. Ali, A., Schnake, T., Eberle, O., Montavon, G., Müller, K.R., Wolf, L.: Xai for transformers: Better explanations through conservative propagation. In: International conference on machine learning. pp. 435–451. PMLR (2022)
4. Ameisen, E., Lindsey, J., Pearce, A., Gurnee, W., Turner, N.L., Chen, B., Citro, C., Abrahams, D., Carter, S., Hosmer, B., et al.: Circuit tracing: Revealing computational graphs in language models. *Transformer Circuits Thread* **6**, 16318–16352 (2025)
5. Bahador, N.: Mechanistic interpretability of fine-tuned vision transformers on distorted images: Decoding attention head behavior for transparent and trustworthy ai. arXiv preprint arXiv:2503.18762 (2025)
6. Bereska, L., Gavves, E.: Mechanistic interpretability for ai safety—a review. arXiv preprint arXiv:2404.14082 (2024)
7. Bhaskar, A., Wettig, A., Friedman, D., Chen, D.: Finding transformer circuits with edge pruning. *Advances in Neural Information Processing Systems* **37**, 18506–18534 (2024)
8. Bricken, T., Templeton, A., Batson, J., Chen, B., Jermyn, A., Conerly, T., Turner, N.L., Anil, C., Denison, C., Askell, A., Lasenby, R., Wu, Y., Kravec, S., Schiefer, N., Maxwell, T., Joseph, N., Tamkin, A., Nguyen, K., McLean, B., Burke, J.E., Hume, T., Carter, S., Henighan, T., Olah, C.: Towards monosemanticity: Decomposing language models with dictionary learning. *Transformer Circuits Thread* (oct 2023), <https://transformer-circuits.pub/2023/monosemantic-features>
9. Bussmann, B., Leask, P., Nanda, N.: Batchtopk sparse autoencoders. arXiv preprint arXiv:2412.06410 (2024)
10. Cammarata, N., Goh, G., Carter, S., Schubert, L., Petrov, M., Olah, C.: Curve detectors. *Distill* **5**(6), e00024–003 (2020)
11. Cao, S., Sanh, V., Rush, A.M.: Low-complexity probing via finding subnetworks. In: Proceedings of the 2021 Conference of the North American Chapter of the Association for Computational Linguistics: Human Language Technologies. pp. 960–966 (2021)
12. Chefer, H., Gur, S., Wolf, L.: Transformer interpretability beyond attention visualization. In: Proceedings of the IEEE/CVF conference on computer vision and pattern recognition. pp. 782–791 (2021)
13. Conmy, A., Mavor-Parker, A., Lynch, A., Heimersheim, S., Garriga-Alonso, A.: Towards automated circuit discovery for mechanistic interpretability. *Advances in Neural Information Processing Systems* **36**, 16318–16352 (2023)
14. Cunningham, H., Ewart, A., Riggs, L., Huben, R., Sharkey, L.: Sparse autoencoders find highly interpretable features in language models. arXiv preprint arXiv:2309.08600 (2023)
15. Dosovitskiy, A., Beyer, L., Kolesnikov, A., Weissenborn, D., Zhai, X., Unterthiner, T., Dehghani, M., Minderer, M., Heigold, G., Gelly, S., et al.: An image is worth 16x16 words: Transformers for image recognition at scale. arXiv preprint arXiv:2010.11929 (2020)

16. Elhage, N., Hume, T., Olsson, C., Schiefer, N., Henighan, T., Kravec, S., Hatfield-Dodds, Z., Lasenby, R., Drain, D., Chen, C., et al.: Toy models of superposition. arXiv preprint arXiv:2209.10652 (2022)
17. Elhage, N., Nanda, N., Olsson, C., Henighan, T., Joseph, N., Mann, B., Askell, A., Bai, Y., Chen, A., Conerly, T., et al.: A mathematical framework for transformer circuits. *Transformer Circuits Thread* **1**(1), 12 (2021)
18. Fawcett, T.: An introduction to roc analysis. *Pattern recognition letters* **27**(8), 861–874 (2006)
19. Frankle, J., Carbin, M.: The lottery ticket hypothesis: Finding sparse, trainable neural networks. arXiv preprint arXiv:1803.03635 (2018)
20. Frantar, E., Alistarh, D.: Sparsegpt: Massive language models can be accurately pruned in one-shot. In: *International conference on machine learning*. pp. 10323–10337. PMLR (2023)
21. Fry, H.: Towards multimodal interpretability: Learning sparse autoencoders for CLIP (2024), <https://www.lesswrong.com/posts/bCtbuWraqYTDtuARg/towards-multimodal-interpretability-learning-sparse-2>, lessWrong
22. Gao, L., Rajaram, A., Coxon, J., Govande, S.V., Baker, B., Mossing, D.: Weight-sparse transformers have interpretable circuits. arXiv preprint arXiv:2511.13653 (2025)
23. Gao, L., la Tour, T.D., Tillman, H., Goh, G., Troll, R., Radford, A., Sutskever, I., Leike, J., Wu, J.: Scaling and evaluating sparse autoencoders. arXiv preprint arXiv:2406.04093 (2024)
24. Han, S., Mao, H., Dally, W.J.: Deep compression: Compressing deep neural networks with pruning, trained quantization and huffman coding. arXiv preprint arXiv:1510.00149 (2015)
25. Marks, S., Rager, C., Michaud, E.J., Belinkov, Y., Bau, D., Mueller, A.: Sparse feature circuits: Discovering and editing interpretable causal graphs in language models. arXiv preprint arXiv:2403.19647 (2024)
26. Nanda, N.: Attribution patching: Activation patching at industrial scale, mar 2023a. URL <https://www.alignmentforum.org/posts/gtLLBhzQTG6nKTeCZ/attribution-patching-activation-patching-at-industrial-scale>
27. Olah, C., Cammarata, N., Schubert, L., Goh, G., Petrov, M., Carter, S.: Zoom in: An introduction to circuits. *Distill* **5**(3), e00024–001 (2020)
28. Olsson, C., Elhage, N., Nanda, N., Joseph, N., DasSarma, N., Henighan, T., Mann, B., Askell, A., Bai, Y., Chen, A., et al.: In-context learning and induction heads. arXiv preprint arXiv:2209.11895 (2022)
29. Rajamanoharan, S., Conmy, A., Smith, L., Lieberum, T., Varma, V., Kramár, J., Shah, R., Nanda, N.: Improving dictionary learning with gated sparse autoencoders. arXiv preprint arXiv:2404.16014 (2024)
30. Rajamanoharan, S., Lieberum, T., Sonnerat, N., Conmy, A., Varma, V., Kramár, J., Nanda, N.: Jumping ahead: Improving reconstruction fidelity with jumprelu sparse autoencoders. arXiv preprint arXiv:2407.14435 (2024)
31. Samek, W., Binder, A., Montavon, G., Lapuschkin, S., Müller, K.R.: Evaluating the visualization of what a deep neural network has learned. *IEEE transactions on neural networks and learning systems* **28**(11), 2660–2673 (2016)
32. Schubert, L., Voss, C., Cammarata, N., Goh, G., Olah, C.: High-low frequency detectors. *Distill* **6**(1), e00024–005 (2021)
33. Sun, M., Liu, Z., Bair, A., Kolter, J.Z.: A simple and effective pruning approach for large language models. arXiv preprint arXiv:2306.11695 (2023)

34. Takatsuki, R., Joseph, S., Fujisawa, I., Kanai, R.: Decoding vision transformers: the diffusion steering lens. In: Proceedings of the Computer Vision and Pattern Recognition Conference. pp. 4819–4824 (2025)
35. Templeton, A.: Scaling monosemanticity: Extracting interpretable features from claude 3 sonnet. Anthropic (2024)
36. Touvron, H., Cord, M., Jégou, H.: Deit iii: Revenge of the vit. In: European conference on computer vision. pp. 516–533. Springer (2022)
37. Vig, J., Gehrmann, S., Belinkov, Y., Qian, S., Nevo, D., Sakenis, S., Huang, J., Singer, Y., Shieber, S.: Causal mediation analysis for interpreting neural nlp: The case of gender bias. arXiv preprint arXiv:2004.12265 (2020)
38. Voss, C., Cammarata, N., Goh, G., Petrov, M., Schubert, L., Egan, B., Lim, S.K., Olah, C.: Visualizing weights. Distill **6**(2), e00024–007 (2021)
39. Wang, K., Variengien, A., Conmy, A., Shlegeris, B., Steinhardt, J.: Interpretability in the wild: a circuit for indirect object identification in gpt-2 small, 2022. URL <https://arxiv.org/abs/2211.00593> **2** (2022)
40. Zimmermann, R.S., Klein, T., Brendel, W.: Scale alone does not improve mechanistic interpretability in vision models. Advances in Neural Information Processing Systems **36**, 57876–57907 (2023)

A Technical Implementation Details

In this section, we provide the specific technical configurations and architectural adaptations used for the IMPACT framework, ensuring the reproducibility of our multi-level interpretability analysis.

A.1 Differentiable Circuit Discovery

To identify minimal functional subgraphs, we utilize a learnable binary masking approach. Because the Heaviside step function is non-differentiable, we implement a **Sigmoid Gradient Estimator** for the backward pass. During the forward pass, mask logits m are thresholded at zero to ensure the model evaluates a strictly binary circuit. During backpropagation, we utilize a surrogate gradient to enable AdamW optimization:

$$\frac{\partial \hat{m}}{\partial m} = \tau \cdot \sigma(\tau m)(1 - \sigma(\tau m)) \quad (13)$$

where τ is the temperature hyperparameter (set to 1.0). All mask logits are initialized with Gaussian noise ($\mu = 0.5, \sigma = 0.01$) and clamped to the $[-1, 1]$ range after each step to maintain gradient sensitivity.

Fused QKV Handling: The DeiT-III architecture utilizes fused QKV linear layers. To allow for granular circuit analysis, our framework manually slices the fused output into three distinct tensors (Q, K, V). Unlike the MLP layers, which use per-feature masking, we apply **per-head masking** to the $Q, K,$ and V projections independently. This allows the framework to determine if specific attention components (e.g., the Query of a specific head) are functionally redundant for the target class.

A.2 Neuron-Level Metric Implementation

Our neuron-level analysis is designed to be robust to the spatial and structural properties of Vision Transformers.

Spatial Invariance via Max-Pooling: For *Class Variance* and *Label Entropy*, we address the spatial nature of patch tokens. Rather than averaging activations across the image, we apply a **Max-Pooling** strategy across the patch tokens (1 : 197) for each image. This identifies if a feature is detected *anywhere* in the spatial field, ensuring metrics are translation-invariant and reflect semantic content rather than spatial coordinates.

Attention Head Quantization: To compare attention layers with MLP neurons, we treat each attention head as a single unit. The activation of a head is defined as the L_2 **norm** of its output across the head dimension ($D = 64$). This allows for a direct comparison of head-level selectivity against individual MLP neuron selectivity.

A.3 Model Adaptation for Transformer Attribution

To maintain mathematical consistency during relevance propagation in Section 3.5, we adapted the DeiT-III architecture to the Layer-wise Relevance Propagation (LRP) framework.

LayerScale-Aware Relprop: DeiT-III introduces *LayerScale*, applying learned diagonal scaling (γ) to sub-block outputs. We dynamically patched the transformer blocks to include *LayerScale-aware relprop* rules. This ensures that the relevance R back-propagated through a scaled sub-block is correctly weighted by the learned parameters:

$$R_{in} = R_{out} \cdot (\gamma + \epsilon)^{-1} \quad (14)$$

Structural Synchronization: We performed two additional modifications:

- **QKV Decoupling**: The fused QKV projections were decoupled into separate linear layers. The V weight matrix was synchronized to a standalone `v_proj` module, which is required by the constrained propagation rules (CP-rule) to prevent relevance leakage through the attention mechanism.
- **Position Embedding Padding**: We expanded the `pos_embed` from 196 to 197 tokens by prepending a zero-initialized row, accommodating the CLS token index expected by the LRP generator.

A.4 Ablation Methodology

We employ **Mean Ablation** across all internal experiments to avoid out-of-distribution artifacts. We first precompute the dataset-wide mean activation for 96 hook points (8 per block). During neuron-level impact analysis and circuit discovery, inactive units are replaced by these precomputed means rather than being zeroed out.

B SAE Hyperparameter Selection and Future Adaptive Strategies

To identify the optimal analytical probe for the IMPACT framework, we performed a sweep across token types, sparsity levels (k), and expansion factors on the dense DeiT-III B/16 model. To ensure a fair, controlled comparison across the sparsity spectrum, we utilize the *identical* SAE configuration for all sparse variants.

Dense Baseline Selection. As shown in Table 5, the **CLS token** at Block 11 serves as a high-fidelity semantic bottleneck, explaining over 99.2% of the variance. We identified $k = 128$ and an expansion factor of 32 as the *saturation point* for the dense model, where further increases in dictionary size provide diminishing returns in NMSE. This configuration was selected as our standardized analytical probe.

Future Work: Adaptive SAE Configurations. While our primary analysis uses a fixed probe to isolate model changes, Table 6 illustrates that the optimal SAE setup may shift as weight-sparsity increases. Specifically, in the 70% sparse model, increasing k to 256 yields a significant improvement in NMSE (0.0569 \rightarrow 0.0318). This suggests that sparse models may require a higher number of active latents to reconstruct their representations faithfully, likely due to the *representation spreading* effect. We leave the development of model-aware, adaptive SAE architectures as a subject for future research.

Table 5: SAE reconstruction metrics for the dense DeiT-III B/16 Block 11 activations. The selected configuration (**bold**) represents the saturation point for semantic reconstruction.

Tokens	k	Expansion Factor	FVE \uparrow	NMSE \downarrow
CLS	128	16	0.9925	0.0075
CLS	128	32	0.9926	0.0074
CLS	128	64	0.9926	0.0074
CLS	32	32	0.9869	0.0131
CLS	64	32	0.9898	0.0102
CLS	256	32	0.9949	0.0051
All	128	32	0.9476	0.0524
Patch	128	32	0.9474	0.0526

Table 6: SAE reconstruction across Wanda-pruned models. These sweeps provide evidence for the potential benefits of adaptive SAE configurations in future work.

Model	Tokens	k	Expansion Factor	FVE \uparrow	NMSE \downarrow
Wanda 0.3	CLS	128	16	0.9619	0.0381
Wanda 0.3	CLS	128	32	0.9618	0.0382
Wanda 0.3	CLS	256	32	0.9781	0.0219
Wanda 0.5	CLS	128	16	0.9557	0.0443
Wanda 0.5	CLS	128	32	0.9554	0.0446
Wanda 0.5	CLS	256	32	0.9747	0.0253
Wanda 0.7	CLS	128	16	0.9435	0.0565
Wanda 0.7	CLS	128	32	0.9431	0.0569
Wanda 0.7	CLS	256	32	0.9682	0.0318

C Circuit Discovery: Architecture and Optimization

The extraction of task-specific functional subgraphs provides a macro-level view of how model sparsity affects computational modularity. This section details the differentiable masking framework and the empirical rationale for our hyperparameter selection.

C.1 Differentiable Masking Framework

For each transformer block, we insert learnable binary masks at eight strategic locations: `norm1`, `q`, `k`, `v`, `attn_out`, `norm2`, `mlp_act`, and `mlp_out`. To enable gradient-based optimization of these discrete masks, we employ a **Heaviside Step Function** during the forward pass and a **Sigmoid Gradient Estimator** during the backward pass:

$$\hat{m} = \mathbb{I}(m > 0), \quad \frac{\partial \hat{m}}{\partial m} = \tau \cdot \sigma(\tau m)(1 - \sigma(\tau m)) \quad (15)$$

where m represents the continuous mask logits and $\tau = 1.0$ is the temperature. We initialize mask logits from a Gaussian distribution $\mathcal{N}(0.5, 0.01)$ and apply clamping to the range $[-1, 1]$ after each update to maintain optimization stability.

Fused QKV and Attention Slicing: To account for the fused *QKV* linear layers in DeiT-III, we manually slice the projection output to apply separate **per-head masks** for the Query, Key, and Value components. This granularity allows the IMPACT framework to isolate specific attention heads that may be redundant for a given classification task even if other heads in the same block remain active.

C.2 Hyperparameter Selection and k -Scaling

Given the computational cost of circuit extraction across 100 ImageNet categories, we utilized a two-stage process to identify robust hyperparameters. A pilot study using Bayesian optimization (CARBS) on 20 categories identified a stable region for the dense baseline: a learning rate of 10^{-2} , a sparsity coefficient $k = 8 \times 10^{-5}$, and an optimization schedule of 15 epochs using a `StepLR` scheduler ($\gamma = 0.2$).

Sensitivity and Circuit Collapse: We observed that sparse models are significantly more sensitive to regularization pressure. As shown in Table 7, applying the dense model’s penalty (8×10^{-5}) to the Wanda 70% variant results in a 6.6% drop in circuit accuracy and significantly higher variance ($\pm 10.89\%$). This phenomenon, which we term “circuit collapse,” occurs when the optimization pressure exceeds the representational capacity of the remaining weights.

By scaling the penalty to $k = 4 \times 10^{-5}$ for the sparse variants, we achieve a 9.3× reduction in standard deviation and a peak in *Normalized Circuit Quality* (NCQ). This ensures that our cross-model comparisons are based on the most stable and faithful circuits possible for each architecture.

Table 7: Sensitivity of circuit extraction to the sparsity coefficient (k) for the Wanda 70% model. Results are averaged over 100 ImageNet categories. The selected coefficient (**bold**) maximizes both Accuracy and NCQ.

k Coefficient	Node (%) ↓	Size (%) ↓	Acc. (%) ↑	NCQ ↑
4e-05	41.60 ± 2.23	12.94 ± 0.58	89.64 ± 6.22	0.7804 ± 0.054
5e-05	46.19 ± 3.54	14.49 ± 0.86	89.33 ± 8.39	0.7637 ± 0.071
6e-05	43.71 ± 3.29	13.86 ± 0.76	87.69 ± 8.80	0.7552 ± 0.075
7e-05	33.12 ± 5.44	11.08 ± 1.39	83.77 ± 10.02	0.7449 ± 0.090
8e-05	40.04 ± 2.90	12.99 ± 0.62	83.03 ± 10.89	0.7223 ± 0.094

C.3 Evaluation of Functional Fidelity

We evaluate the functional fidelity of the discovered circuits using a balanced binary classification task. For a target category c , the circuit must correctly distinguish between images of class c and images from other classes. The *Ablated Accuracy* of 50% across all experiments serves as a critical validation of our methodology; it demonstrates that removing the discovered circuit returns the model to a random-chance baseline for that specific class. This confirms that the IMPACT framework successfully isolates the primary computational pathways required for class-specific inference.